

# HIVE-Net: Centerline-Aware Hierarchical View-Ensemble Convolutional Network for Mitochondria Segmentation in EM Images

Zhimin Yuan<sup>a</sup>, Xiaofen Ma<sup>b</sup>, Jiajin Yi<sup>a</sup>, Zhengrong Luo<sup>a</sup>, Jialin Peng<sup>a,c,1</sup>

<sup>a</sup>College of Computer Science and Technology, Huaqiao University, Xiamen 361021, China

<sup>b</sup>Department of Medical Imaging, Guangdong Second Provincial General Hospital, Guangzhou, 510317, China

<sup>c</sup>Xiamen Key Laboratory of Computer Vision and Pattern Recognition, Huaqiao University, Xiamen 361021, China

## Abstract

**Background and objective:** With the advancement of electron microscopy (EM) imaging technology, neuroscientists can investigate the function of various intracellular organelles, e.g. mitochondria, at nano-scale. Semantic segmentation of electron microscopy (EM) is an essential step to efficiently obtain reliable morphological statistics. Despite the great success achieved using deep convolutional neural networks (CNNs), they still produce coarse segmentations with lots of discontinuities and false positives for mitochondria segmentation.

**Methods:** In this study, we introduce a centerline-aware multitask network by utilizing centerline as an intrinsic shape cue of mitochondria to regularize the segmentation. Since the application of 3D CNNs on large medical volumes is usually hindered by their substantial computational cost and storage overhead, we introduce a novel hierarchical view-ensemble convolution (HVEC), a simple alternative of 3D convolution to learn 3D spatial contexts using more efficient 2D convolutions. The HVEC enables both decomposing and sharing multi-view information, leading to increased learning capacity.

**Results:** Extensive validation results on two challenging benchmarks show that, the proposed method performs favorably against the state-of-the-art methods in accuracy and visual quality but with a greatly reduced model size. Moreover, the proposed model also shows significantly improved generalization ability, especially when training with quite limited amount of training data. Detailed sensitivity analysis and ablation study have also been conducted, which show the robustness of the proposed model and effectiveness of the proposed modules.

**Conclusions:** The experiments highlighted that the proposed architecture enables both simplicity and efficiency leading to increased capacity of learning spatial contexts. Moreover, incorporating shape cues such as centerline information is a promising approach to improve the performance of mitochondria segmentation.

**Keywords:** Electron microscopy, Image segmentation, Multi-task learning, Centerline Detection

## 1. Introduction

Mitochondria, as the powerhouse of cell, are essential sub-cellular organelles in cell's life cycle. An increasing number of studies have shown that the shape and distribution of mitochondria are closely related to neurodegenerative diseases [4] [24]. Nowadays, with the advancement of electron microscopy (EM) imaging technology, neuroscientists can investigate the function of various intracellular organelles under high-resolution EM images at nano-scale. Accurate delineation of mitochondria in EM images is the prerequisite step for the quantitative analysis of its morphology and distributions. However, manual delineation of such high-resolution data is time-consuming, tedious, subjective and also has limited reproducibility [27]. Most importantly, biomedical images must be annotated by experts which are more costly than annotating natural images.

Consequently, fully automated mitochondria segmentation algorithms with sufficient accuracy are valuable to help neurologist analyze EM images. Unfortunately, in virtue of the irregular shape variance, shift size, fuzzy boundaries of mitochondria and its complex background in EM images, as shown in Fig. 1, mitochondria segmentation has proven to be a challenging task.

A variety of studies have introduced kinds of specially-designed hand-crafted features [26, 32, 19, 31, 2] for mitochondria segmentation, which are usually combined with classical machine learning algorithms [26, 22, 31, 21], e.g., random forest [26, 31], AdaBoost [2], conditional random fields (CRF) [21, 22]. Despite the sound performance, approaches in this class have shown limited ability to address the substantial increase of data scale, due to the limited representability of hand-crafted features and small capacity of classical shallow machine learning models.

Recently, fully convolutional neural network (FCN), has gained remarkable performance for biomedical image segmentation [30, 6, 13, 40]. Generally, building deeper and wider networks, also allowing a large input size, is crucial to achieve higher accuracy for the challenging segmentation task. A strong

\*This work was supported in part by National Natural Science Foundation of China (No.11771160), and Science and Technology Project of Fujian Province (No. 2019H0016).

Email address: 2004pj1@163.com (Jialin Peng)

<sup>1</sup>Corresponding author.

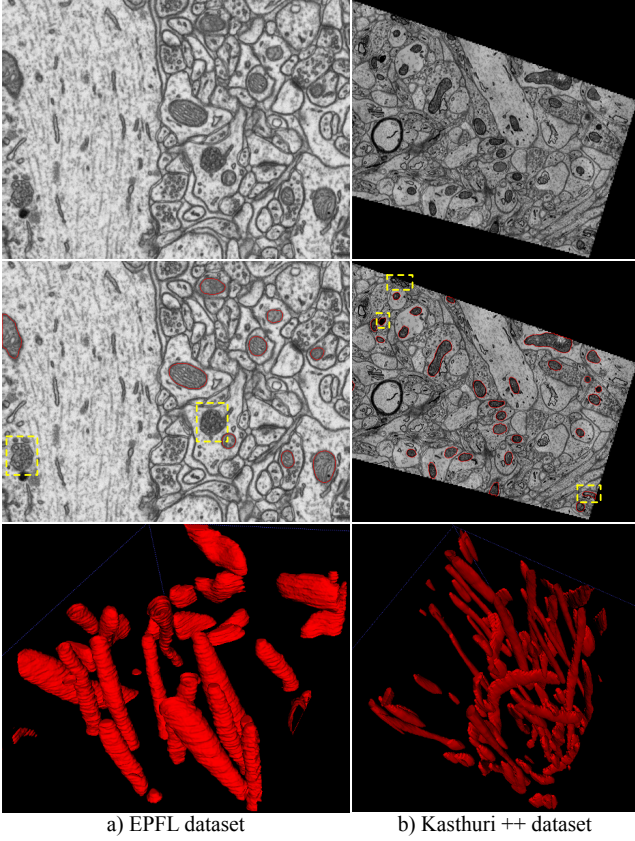


Figure 1: Illustration of challenging examples for mitochondria segmentation. First row: EM images; Second row: corresponding segmentation ground-truth (red contours); Third row: 3D visualization of ground truth. Some error-prone locations are highlighted with dotted boxes.

baseline network for medical image segmentation is the U-Net [30, 6], which is a typical 2D FCN using encoder-decoder architecture and skip connections. For EM segmentation, existing studies [1, 34, 3, 8, 38] are mainly based on the U-Net-like architecture and its 3D variants 3D U-Net [6] and V-Net [23]. Given a volume image, 2D networks process it slice by slice. Despite its computational efficiency, the 2D segmentation network usually cannot achieve competitive segmentation performance, because the inter-slice information is completely omitted. In contrast, networks using 3D convolutions have shown state-of-the-art results for medical volume segmentation by taking advantage of full spatial contexts. One limitation of the 3D FCN is the significantly increased number of learning parameters with 3D convolution kernel, which inevitably brings high computational cost. Due to GPU memory restrictions, 3D FCNs usually adopt small-scale sliding volumes to process the original large volume. The high GPU memory consumption of 3D FCNs also limits the network depth compared to that of 2D FCNs. With large parameter space, most deep-learning based algorithms, especially deep 3D FCN models, require a vast amount of manually annotated training data which is hard to collect in clinical usage. Recently, Xie et al.[36] proposed to predict the segmentation errors produced by an existing model and then correct them with a verification network.

Besides segmentation accuracy, computation complexity is another important consideration for model design. Since huge scale of parameters and high computational cost will inevitably make a model prohibitive on devices with limited GPU memory or application on dataset of limited size. A typical solution for light-weight architecture design is to explore low rank factorization of convolutional kernels [5, 33, 35]. For EM image segmentation, Cheng *et al.* [3] approximated a 3D convolution with three successive rank-1 (1D) kernels, which can greatly reduce the model parameters. However, the 1D convolutions have limited ability to capture crucial 3D spatial context. In fact, incorporating full spatial context and multi-scale features are critical, especially for addressing challenging tasks using light-weight models, since EM images are cluttered with structures exhibiting similar intensities and textures, and strong gradients do not necessarily indicate the semantic boundaries of mitochondria. Therefore, devising a model not only effective to capture discriminative context but also efficient under strict memory and computational budget constraints is our focus.

To address the shortcomings mentioned above, we propose a multi-task pseudo-3D network, named *HIVE-Net*, which can not only utilize intrinsic shape cues to regularize the semantic segmentation task, but also exploit 3D spatial contexts using only 2D convolutions. Specifically, we integrate two closely related tasks, i.e. segmentation and centerline detection into a single network. The objective is to take account of the intrinsic shape cue of mitochondria represented by centerline to help improve the generalization performance and robustness of the segmentation model, especially when only scarce annotated training samples are available.

Moreover, a novel *hierarchical view-ensemble convolution* (HVEC) module shown in Fig. 3 is introduced to reduce learning parameters and computation cost, and take advantage of the multi-view property of a 3D volume. This is based on the observation that a blurred boundary on one cross-section (view) of a 3D volume, may be easily delineated on other two cross sections, which is demonstrated in Fig. 4. Note that the proposed strategy is completely different from the widely-used multi-view ensemble strategy [13, 40], which finally fuses independent 2D segmentations on three view with voting or averaging. In contrast, we focus on hierarchically extract multi-view contexts to boost the discriminative ability of the learned features. The difference between the proposed HVEC and other group convolutions strategies [9, 33] lies in that, we firstly decouple a 3D spatial convolution into multiple 2D spatial convolutions, and then apply different 2D convolutions on different channel groups with a focal view. Extensive evaluations of the proposed method have been made on two public benchmarks.

The main contributions of our study can be summarized by the following threefold,

- We propose to use intrinsic shape cues to boost the segmentation accuracy and generalization ability, and have developed a novel centerline-aware segmentation network.
- To achieve a light-weight network for 3D segmentation, we introduce a novel HVEC module, a simple alternative

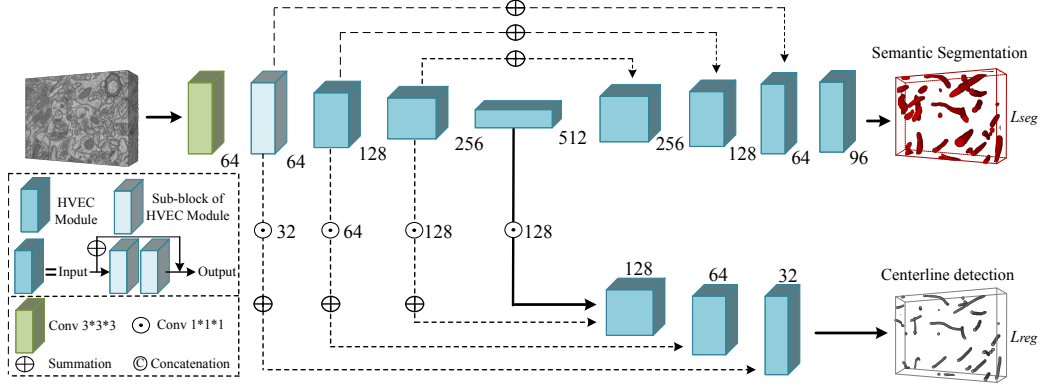


Figure 2: Overall architecture of our HIVE-Net, which integrates two closely related tasks, for 3D segmentation of mitochondria. The centerline detection branch is utilized to encode intrinsic shape knowledge, and suppress discontinuities and false positives in the segmentation. A novel HVEC module involving only 2D convolutions, is the basic building blocks, which are represented by colored cubes with numbers below being the number of feature channels. Each HVEC module consists of two HVECs as sub-blocks with short connection cross them for residual learning.

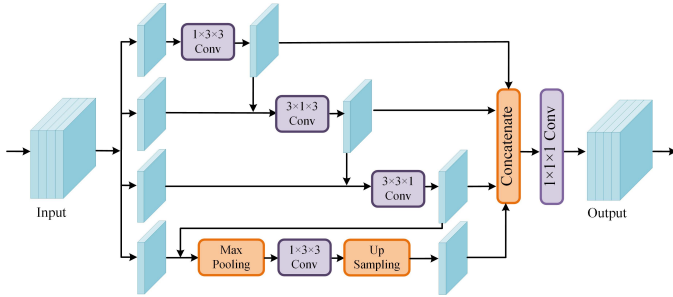


Figure 3: The multi-branch architecture of our *hierarchical view-ensemble convolution* (HVEC). In order to extract multi-view multi-scale contextual features, we perform in parallel three different rank-2 (2D) spatial convolutions, corresponding to operating on the three orthogonal views of a 3D volume, on different subgroups of feature channels with hierarchical connections. The fourth branch is to extract multi-scale contextual features on one focal view.

of 3D convolution to learn 3D spatial contexts using only 2D convolutions, to reduce the number of parameters and facilitate multi-view information aggregation.

- Very promising performance, even with quite limited training data, in comparison with state of the arts has been obtained by using the proposed HIVE-Net network on two publicly available benchmarks.

This work is an extension of our preliminary work [37] with validations on more datasets and more extensive experiments on performance analysis, including the evaluation of the ability of instance-level segmentation and detection. Ablation study of our model and sensitivity analysis of tradeoff hyper-parameter are also conducted. More comprehensive review of close-related literature and detailed discussion of our motivation have also been included.

The reminder of this paper is arranged as follows. We review the related work in Section 2, and describe the proposed methods in Section 3. Dataset details, experimental results and discussions are introduced in Section 4. Section 5 concludes this paper.

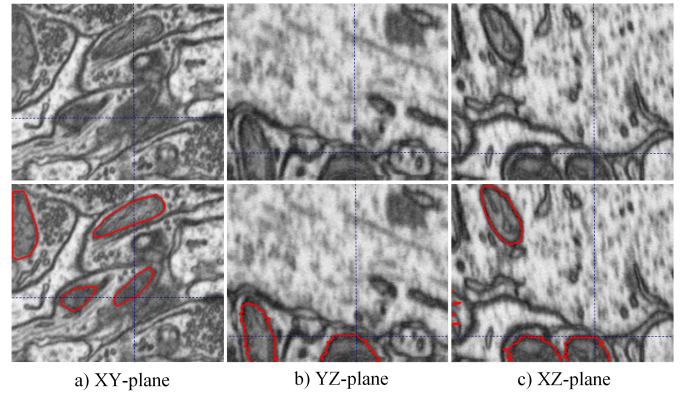


Figure 4: Illustration of the multi-view property of a 3D volume. A volumetric image can be represented in its three dimensions using multi-planar representation. The mitochondria with blurred boundary in the XY-plane, which can be clearly discriminated in other two planes. The ground truth boundaries are the red contours. The axes are shown with blue lines.

## 2. Related Work

**Methods based on hand-crafted features** mainly rely on the extraction of highly discriminating features and a powerful classifier to automatically determine the presence of mitochondria and delineate their boundaries accurately. Beyond of using general texture features from computer vision studies [2], recent studies have introduced specially-designed geometrical and contextual features for mitochondria segmentation, such as ray features [32, 22], Radon-like features [19], local patch pattern [26], etc, which have shown greatly improved discriminative ability [26, 22]. Given the features, shallow machine learning algorithms such as Random forest, AdaBoost, etc, are usually adopted for independent pixel-wise labeling. To capture label dependencies between neighboring pixels/voxels, conditional random fields (CRF) with manually-specified or learned parameters are usually employed. However, CRF based methods are typically computationally demanding for volume data. In order to overcome the drawbacks of shallow models and independent pixel-wise labeling, Peng *et al.* [26] introduced a

cascade of structured contextual forest with novel skip connections and integrated multi-view information to exploit contextual feature encoded in spatial-temporal predictions. Despite the competitive performance, hand-crafted features yet showed the limited representability, and the shallow classifiers demonstrated limited learning capacity for large scale data. Furthermore, methods using iterative refinement learning [26] inevitably result in high computational complexity.

**Methods based on deep representation learning** typically performs end-to-end segmentation using FCNs, and have achieved remarkable improvement in performance. A higher performing successor is the U-Net [30], which uses skip connections to exploit multi-scale features. Casser *et al.* [1] proposed a modified 2D U-Net for mitochondria segmentation with on-the-fly data augmentation and reduced depth. Their method, however, did not take full advantage of 3D spatial context, which is crucial for medical volume segmentation. Xiao *et al.* [34] proposed a fully residual U-Net using 3D convolution kernel and deep supervision, which has achieved the state-of-the-art performance. Despite the superior performance of 3D convolutional networks, they bring a significant increase of model parameters, thus need massive labeled data for good performance. For liver segmentation, Zhang *et al.* [39] introduced a hybrid network that used 2D convolutions at the bottom of the encoder to decrease the complexity and 3D convolutions in other layers to explore full spatial context. Moreover, they introduced the depthwise and spatiotemporal separate factorization for 3D convolutions to further reduce complexity. Cheng *et al.* [3] introduced a light-weight 3D residual convolutional network by approximating a 3D convolution with three 1D kernels. Modified residual connections with the stochastic down-sampling, are used to achieve feature-level data augmentation. Although using this factorized 3D kernel can greatly reduce model parameters, the 1D convolutions have limited ability to capture crucial 3D spatial context.

**Separable convolution** is a powerful strategy for the trade-off of light-weight architecture design and better accuracy. A standard convolution conducts computation simultaneously across the spatial dimensions and the channel dimension. *Depthwise separable convolution* strategy [5] independently performs cross-channel convolution and spatial convolution. In contrast, *group convolution* strategies [35, 33], perform convolutions on non-overlapping groups of the feature channels at each layer of a network. Specifically, with channel groups, parallel filters are performed on different filter groups. Further, in [9] connections are added between different filter groups. In aspect of spatial separation, Inception-V3 [33] performs spatial factorization into asymmetric convolutions, e.g. a  $3 \times 3$  convolution is replaced with a  $3 \times 1$  convolution followed by a  $1 \times 3$  convolution. In [29], a 3D convolution is replaced with consecutive 2D and 1D convolutions. Instead of using the aforementioned factorization [33, 9, 29], we perform different rank-2 (2D) spatial convolutions ( $1 \times 3 \times 3$ ,  $3 \times 1 \times 3$ ,  $3 \times 3 \times 1$ ) in parallel on different filter groups to approximate a 3D spatial convolution as depicted in Fig. 3, which captures full spatial context through hierarchically utilizing information from three views. The idea of simultaneously using 2D convolutions of different

orientation was early used also in [28]. A recent work [10] also used parallel 2D convolutions in different orientations for video and volumetric data understanding. However, our proposed architecture is obviously different from their methods. Specifically, we perform hierarchical view-ensemble convolution with inter-connections between parallel branches and additional down-sampled branch. In this way, we can not only take advantage of multi-range field-of-view on a focal view, but also exploit the correlation between different views.

### 3. METHOD

#### 3.1. HIVE-Net

The architecture of our proposed Hierarchical View-Ensemble Convolutional Network (HIVE-Net) for 3D segmentation of mitochondria is shown in Fig. 2. Our method comprises a main task for semantic 3D segmentation as well as an auxiliary centerline detection task to account for the shape information of mitochondria. We formulate the segmentation task as a voxel-wise labeling problem, and the task of centerline detection as a regression problem.

We use the skip-connected encoder-decoder architecture as (3D) U-Net [6, 30], but utilize only one shared encoder and two task-specific decoders, where each decoder accounts for one task. More importantly, other than using 3D convolution, we propose a novel *Hierarchical View-Ensemble Convolution* (HVEC) (Fig. 3) as the building block for both the encoder and decoder, which will be introduced in detail in Section 3.2.

The encoder of the proposed HIVE-Net has  $d$  ( $=3$ ) down-sampling stages to extract multi-scale feature maps in gradually reduced size and capture higher semantic information at later stages. Each decoder has  $d$  ( $=3$ ) up-sampling stages to gradually recover the detailed information about segmentation. With the help of the decoders, low resolution feature maps are progressively restored to the input image size. For the down-sampling operation, we use max-pooling, and for the up-sampling, we use trilinear interpolation. Skip-connections are used to integrate low level cues from the encoder to the corresponding layers of decoder. Instead of using concatenation as U-Net, we use sum operation to achieve long-range residual learning [12]. In fact, concatenation-based operation inevitably increases the number of feature channels, which in turn restricts the input size.

The ground truth for regression is the proximity score map generated using the centerline annotations for the mitochondria, whereas the ground truth for segmentation is the voxel-wise binary labels. The proposed model is trained with the supervision using the following loss,

$$L_{total} = \lambda L_{seg} + (1 - \lambda) L_{reg}, \quad (1)$$

where  $L_{seg}$  and  $L_{reg}$  correspond to the segmentation and regression loss, respectively,  $\lambda$  is a hyper parameter to compromise these two tasks, which is set to 0.7 in the experiments.



### 3.2. HVEC module

Each of our proposed HVEC module has two successive HVECs with residual connection cross them (Fig. 2). In each HVEC shown in Fig. 3, we firstly partition the input features into 4 groups and each group produces its own outputs, which are finally fused with concatenation. Information cross different branches are then integrated with  $1 \times 1 \times 1$  convolutions. Our HVEC module is different from depth-wise and group-wise separable convolutions [33, 9, 35] in four aspects: 1) instead of conducting 3D convolutions on each feature group, we perform different 2D convolutions (i.e.  $1 \times 3 \times 3$ ,  $3 \times 1 \times 3$ ,  $3 \times 3 \times 1$ ) on the first three groups to encode information of three separable orthogonal views of a 3D volume; 2) on the fourth group of features,  $1 \times 3 \times 3$  convolutions are performed on down-sampled features to capture context information at large scale on a focal view; 3) to capture multi-scale contexts and multiple fields-of-view, the four branches are convoluted in serial fashion, and the feature maps convoluted by previous branch are also added to the next branch as input, resulting hierarchical connections; 4) a whole HVEC module consists of two sub-blocks, and shortcut connections across two HVEC sub-blocks are to reformulate it as learning residual function in medium range. Compared with a standard 3D convolution layer attempting to simultaneously learn filters in all the three spatial dimensions and one channel dimension, the proposed factorized scheme is more parameter efficient. In this way, multi-scale and long-range multi-view context information, which are critical to the complicated EM image segmentation, can be encoded in a single module with significantly reduced parameters.

### 3.3. Mitochondria centerline detection

Instead of classifying each voxel as the centerline or the background, we formulate centerline detection as a regression problem [14]. Given the ground truth segmentation, we extract the centerline using a standard software CGAL (Computational Geometry Algorithms Library)<sup>2</sup>. The ground truth for the centerline regression is the proximity score map that is a distance transform function with peak at mitochondria centerlines and zeros on the background. Formally, it is defined as,

$$D(x) = \begin{cases} e^{\alpha(1 - \frac{D_C(x)}{d_M})} - 1, & \text{if } D_C(x) < d_M \\ 0, & \text{otherwise} \end{cases} \quad (2)$$

where  $\alpha$  and  $d_M$  are positive parameters to control the shape of the exponential function, and  $D_C(x)$  represents the minimum Euclidean distance between the voxel  $x$  to the mitochondria centerline. The proximity score map  $D$  is utilized as the supervision to train our centerline detection sub-network. At the end of the detection path, the final feature maps are followed by a Sigmoid layer to get the predicted proximity score map  $D_{out}$ . Minimizing the mean squared error loss  $L_{reg}$  between  $D_{out}$  and  $D$  can accomplish the centerline detection task.

It is noticeable that the number of layers and channels in the detection path is smaller than that in the segmentation. Intuitively, the reasoning for this design is two fold: a) there are

more smaller proportion of voxels taking positive proximity scores than that of voxels taking positive labels. Thus, a deeper and wider network may result in over-fitting; b) increasing the number of feature channels will consume more GPU memory, and in turn decreases the size of network input, which is valuable for accurate segmentation.

### 3.4. Mitochondria segmentation

Compared with the centerline detection path, the segmentation path has one more HVEC module, as shown in Fig. 2. Moreover, the feature maps produced by the last HVEC module in the detection path will be concatenated to the segmentation path. The goal is to take advantage of the location and shape information contained in the detection path. We utilize Jaccard-based loss function which is insensitive to the severe class imbalance in EM data. It is written as,

$$L_{seg} = 1.0 - \frac{\sum_i P_i \cdot Y_i}{\sum_i P_i + \sum_i Y_i - \sum_i P_i \cdot Y_i + \epsilon}, \quad (3)$$

where  $P_i$  is the predicted probability for voxel  $i$  and  $Y_i$  is the corresponding ground truth taking binary label. The small constant  $\epsilon$  (e.g.,  $10^{-5}$ ) is to prevent dividing by zero.

## 4. Results and analysis

### 4.1. Datasets

In this section, we validate the effectiveness of our proposed methods on two public datasets, which are acquired by different electron microscopies and with different voxel spacings.

**EPFL dataset<sup>3</sup>** is the most widely used benchmark for evaluation and consists of two well-annotated stacks for model training and testing. Each stack contains 165 image slices of size  $768 \times 1024$ . These images were acquired by focused ion beam scanning EM (FIB-SEM) and taken from CA1 hippocampus region of the mouse brain with an isotropic resolution of  $5 \text{ nm}^3$  per voxel.

**Kasthuri++ dataset<sup>4</sup>** was firstly released by Kasthuri *et al.* [15] and the annotation of mitochondria was refined by Casser *et al.* [1]. In this dataset, there are 85 image slices of size  $1643 \times 1613$  for training and 75 slices of size  $1334 \times 1553$  images for testing. All images were acquired by serial section EM (ssEM) and taken from 3-cylinder mouse cortex with an anisotropic resolution of  $3 \times 3 \times 30 \text{ nm}$  per voxel.

### 4.2. Evaluation criteria

To measure the agreement between the binary ground truth and automatical segmentation, two evaluation metrics are used, i.e., Dice similarity coefficient (DSC) and Jaccard-index coefficient (JAC). They are defined as,

$$\text{DSC} = \frac{2|P \cap Y|}{|P| + |Y|}, \quad \text{JAC} = \frac{|P \cap Y|}{|P \cup Y|} \quad (4)$$

<sup>2</sup><https://www.cgal.org/>

<sup>3</sup><https://cvlab.epfl.ch/data/em>

<sup>4</sup><https://casser.io/connectomics/>

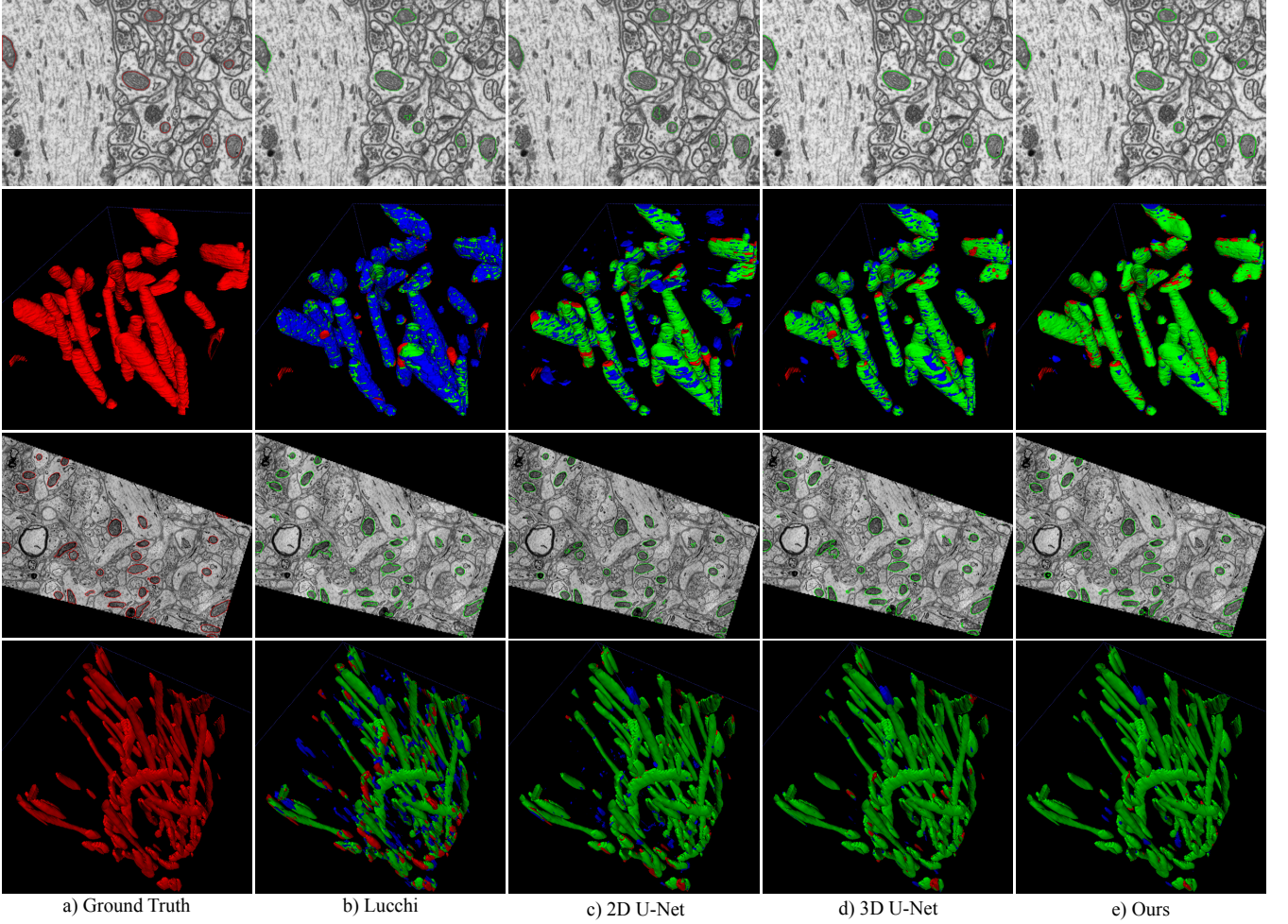


Figure 5: The visual comparison of our segmentation result versus other methods on EPFL dataset (first and second rows) and Kasthuri++ dataset (third and last rows). In the first and third rows, the red contours denote the ground truth, and the green contours denote results of the compared methods. The second and fourth rows are the 3D visualization of the segmentations of each method and the ground truth. The red and blue fragments in columns (b)-(e) are the false negative and false positive predictions, respectively. True positive predictions are denoted by green.

where  $S$  and  $Y$  denote the predicted binary segmentation and ground truth, respectively. These two metrics are widely used as assessment criteria for medical image segmentation.

To evaluate the object-level performance of segmentation, we have also used the aggregated Jaccard-index (AJI) [18] and Panoptic Quality (PQ) [17, 11] as assessment measures. Suppose the  $Y^j$  is the  $j$ th mitochondrion with a total of  $N$  mitochondria, the AJI is defined as follows.

$$\text{AJI} = \frac{\sum_{j=1}^N |Y^j \cap P^{j^*}|}{\sum_{j=1}^N |Y^j \cup P^{j^*}| + \sum_{i \in \text{FP}} |P^i|}, \quad (5)$$

where  $j^*$  is the index of the matched segment (i.e., connected region) in the predicted segmentation  $P$  with the largest overlapping (in terms of JAC) with  $Y^j$ ; FP is the set of false positive regions in  $P$  without the corresponding ground truth mitochondria.

The measure of PQ splits the predicted and ground truth segments into three sets: true positives (TP), false positives (FP), and false negatives (FN), representing the matched pairs of

segments with at least 50% overlapping in JAC, unmatched predicted segments, and unmatched ground truth segments, respectively. Accordingly, PQ is a combination of segmentation quality (SQ) in TP and detection quality (DQ) in terms of F1, and is defined as follows.

$$\text{PQ} = \underbrace{\frac{\sum_{j \in \text{TP}} \text{JAC}(Y^j, P^{j^*})}{|\text{TP}|}}_{\text{Segmentation Quality (SQ)}} \times \underbrace{\frac{|\text{TP}|}{|\text{TP}| + \frac{1}{2}|\text{FP}| + \frac{1}{2}|\text{FN}|}}_{\text{Detection Quality (DQ)}} \quad (6)$$

To measure instance-level detection performance, we use F1, i.e., the DQ in PQ. For completeness, we also conducted several experiments by considering different overlapping thresholds. Moreover, given the numbers of TP and FN, we also report the sensitivity (SEN) and specificity (SPE),

$$\text{SEN} = \frac{|\text{TP}|}{|\text{TP}| + |\text{FN}|}, \quad \text{SPE} = \frac{|\text{TN}|}{|\text{TN}| + |\text{FP}|} \quad (7)$$

We also use the Average Precision (AP) [20], which is a popular metric in measuring detection accuracy. The AP measures

the performance with overlapping of bounding box for a detection to be a true positive. For example, the AP-75 requires at least 75% intersection over union (IoU) with the ground truth for a positive detection. Moreover, we have also illustrated the result with different thresholds, i.e., AP-[50:5:85]. In comparison, AP-65 and AP-75 are strict but proper measures, and AP-85 is too strict.

#### 4.3. Implementation details

We implement our model using Pytorch [25] on a workstation with 64GB RAM and one GTX 1080Ti GPU. The model is optimized by Adam [16] optimizer and the weight decay is set to  $10^{-5}$ . Initial learning rate is set to  $10^{-4}$  and step-wise learning rate decay scheme is employed, where the step and decay rates are set to 15 and 0.9, respectively. We set  $\alpha=3$ , and  $d_M=15$ .

Our network is trained using randomly cropped volumes of size  $40 \times 136 \times 136$  and batch size 1. Instance normalization is used. Data augmentation including sagittal flipping, random transpose and random rotations of  $90^\circ$  is used for model training. At the inference time, we apply test-time augmentation on the isotropic EPFL dataset to further improve the performance, which is widely used in EM image segmentation [34], [7]. For prediction efficiency, the test-time augmentation only includes three rotations of the volume image and averaging all the predictions.

#### 4.4. Performance of binary and instance segmentation

To evaluate the proposed HIVE-Net, we firstly compare it with several state-of-the-art methods on the challenging EPFL dataset, which is the *de facto* standard benchmark for evaluation. Both class-level measures, i.e., DSC and JAC, and instance-level measures, i.e., AJI and PQ, are used for evaluation. These compared methods are: 1) state-of-the-art methods using hand-crafted features including Lucchi *et al.* [21], Cetina *et al.* [2], and Peng *et al.* [26]; 2) strong baseline FCN models including U-Net [30] and 3D U-Net [6]; 3) the light-weight 3D residual convolutional network by Cheng *et al.* [3] using factorized convolutions and online augmentation at the feature-level, which is closely-related with our method, and its 2D variant; 5) the fully 3D residual U-Net by Xiao *et al.* [34] using deep supervision and complex test-time augmentation; 6) variants of the proposed HIVE-Net. For fair comparison, the same data augmentation at training and testing stages as our method is used in the implementation of the compared deep learning based methods.

**Visual comparison.** The visual comparison of our segmentation result versus three baseline methods on both datasets are shown in Fig. 5. As the 3D visualization in the second and fourth rows of Fig. 5 shows, the results of the 2D U-Net demonstrates a appearance with more discontinuities and false positives, due to the fact that the slice-by-slice method lacks spatial consistency between neighboring slices and cannot consider full 3D context of a volumetric image. In contrast, both the 3D U-Net and our pseudo 3D method can account for the spatial consistency between slices, enabling better results with

Table 1: Comparison of different methods for mitochondria segmentation on EPFL dataset. The evaluation results under both class-level measures, i.e., DSC and JAC, and instance-level measures, i.e., AJI and PQ, are reported.

| Methods                      | Class-level |             | Instance-level |             |
|------------------------------|-------------|-------------|----------------|-------------|
|                              | DSC(%)      | JAC(%)      | AJI(%)         | PQ(%)       |
| Lucchi <i>et al.</i> [21]    | 86.0        | 75.5        | 74.0           | 63.5        |
| Cetina <i>et al.</i> [2]     | 86.4        | 76.0        | –              | –           |
| Peng <i>et al.</i> [26]      | 90.9        | 83.3        | 75.4           | 67.7        |
| U-Net [30]                   | 91.5        | 84.4        | 83.0           | 75.5        |
| Cheng <i>et al.</i> (2D) [3] | 92.8        | 86.5        | –              | –           |
| 3D U-Net [6]                 | 93.5        | 87.8        | 86.9           | 80.6        |
| Cheng <i>et al.</i> (3D) [3] | 94.1        | 88.9        | –              | –           |
| Casser <i>et al.</i> [1]     | 94.2        | 89.0        | –              | –           |
| Xiao <i>et al.</i> [34]      | 94.7        | 90.0        | 88.6           | 83.1        |
| HIVE-Net (single task)       | 94.3        | 89.2        | 88.3           | 82.4        |
| HIVE-Net (multi-task)        | <b>94.8</b> | <b>90.1</b> | <b>89.0</b>    | <b>83.9</b> |

Table 2: Comparison of different methods for mitochondria segmentation on Kasthuri++ dataset. The results under both class-level metrics, i.e., DSC and JAC, and instance-level metrics, i.e., AJI and PQ, are reported.

| Methods                   | Class-level |             | Instance-level |             |
|---------------------------|-------------|-------------|----------------|-------------|
|                           | DSC(%)      | JAC(%)      | AJI(%)         | PQ(%)       |
| Lucchi <i>et al.</i> [21] | 86.2        | 75.8        | 73.5           | 57.6        |
| Peng <i>et al.</i> [26]   | 89.3        | 80.6        | 85.8           | 72.9        |
| U-Net [30]                | 94.0        | 88.6        | 87.5           | 80.2        |
| 3D U-Net [6]              | 94.3        | 89.2        | 87.9           | 81.5        |
| Xiao <i>et al.</i> [34]   | 95.9        | 92.2        | 91.0           | 85.1        |
| HIVE-Net (single task)    | 95.7        | 91.7        | 90.4           | 84.7        |
| HIVE-Net (multi-task)     | <b>96.2</b> | <b>92.8</b> | <b>91.5</b>    | <b>86.6</b> |

fewer false positives. Moreover, our method shows more accurate and more smoother results with fewer cracks, and is less memory demanding than 3D U-Net.

**Performance of segmentation.** The comparison results on the EPFL dataset are shown in Table 1. Overall, the algorithms based on deep learning can significantly outperform traditional methods. The performance of both the 3D U-Net and our pseudo 3D method including its single task variant is superior than that of 2D U-Net in all of the four metrics, which further confirms the importance of 3D spatial context and the effectiveness of the multi-view context captured by our HVEC. With additional centerline detection task, we obtain a performance gain of 0.9% in terms of JAC and a performance gain of 0.7% in terms of AJI and 1.5% in PQ. Our full model yields an accuracy of 94.8% in DSC and 90.1% in JAC for binary segmentation and an accuracy of 89.0% in AJI and 83.9% in PQ, which outperform all other methods. These experimental results validate the effectiveness of our HVEC module and the auxiliary detection task which can help improve the robustness and the generalization performance of segmentation task.

The comparison results on Kasthuri++ dataset, which is a dataset with anisotropic spatial resolution, are summarized in Table 2. On this dataset, similar results as that on EPFL dataset

Table 3: Detection performance on EPFL dataset. The evaluation results under DQ (i.e., F1-50), SEN, SPE, AP-65 and AP-75 are reported. The measures DQ, SEN, and SPE are based on measuring the segment overlapping of matched instances, while the AP-65 and AP-75 are based on measuring the bounding-box overlapping of matched instances.

| Methods                   | Segment     |             |             | Bounding-box |             |
|---------------------------|-------------|-------------|-------------|--------------|-------------|
|                           | DQ          | SEN         | SPE         | AP-65        | AP-75       |
| Lucchi <i>et al.</i> [21] | 85.4        | 92.1        | 80.2        | 54.7         | 19.1        |
| Peng <i>et al.</i> [26]   | 88.5        | <b>96.6</b> | 82.2        | 65.5         | 25.5        |
| U-Net [30]                | 88.4        | 93.1        | 84.8        | 64.1         | 60.2        |
| 3D U-Net [6]              | 93.6        | 95.8        | 91.8        | 74.8         | 74.8        |
| Xiao <i>et al.</i> [34]   | 93.4        | 94.7        | 92.5        | 71.3         | 71.3        |
| HIVE-Net (single task)    | 93.4        | <b>96.6</b> | 90.6        | 74.9         | <b>74.9</b> |
| HIVE-Net (multi-task)     | <b>95.0</b> | 96.1        | <b>94.1</b> | <b>77.7</b>  | <b>74.9</b> |

Table 4: Detection performance on Kasthuri++ dataset. The evaluation results under DQ (i.e., F1-50), SEN, SPE, AP-65 and AP-75 are reported.

| Methods                   | Segment     |             |             | Bounding-box |             |
|---------------------------|-------------|-------------|-------------|--------------|-------------|
|                           | DQ          | SEN         | SPE         | AP-65        | AP-75       |
| Lucchi <i>et al.</i> [21] | 68.5        | 79.1        | 60.8        | 40.7         | 27.1        |
| Peng <i>et al.</i> [26]   | 77.9        | <b>95.5</b> | 66.4        | 54.1         | 44.8        |
| U-Net [30]                | 88.0        | 88.8        | 87.8        | 84.3         | 76.6        |
| 3D U-Net [6]              | 90.8        | 92.2        | 89.5        | 79.9         | 73.2        |
| Xiao <i>et al.</i> [34]   | 92.3        | 93.3        | 91.5        | 86.1         | 80.1        |
| HIVE-Net (single task)    | 91.8        | 93.7        | 90.1        | 84.2         | 80.9        |
| HIVE-Net (multi-task)     | <b>93.3</b> | 94.6        | <b>92.2</b> | <b>87.3</b>  | <b>84.2</b> |

have been obtained. Methods using 3D context and multi-view contexts perform better than methods relying on only 2D contexts. More specifically, the experimental results indicate that our model is superior than other approaches. Our model yields an accuracy of 96.2% in DSC and 92.8% in JAC for binary segmentation task, and an accuracy of 91.5% in AJI and 96.6 in PQ for object-level segmentation. With the additional center-line detection task, we obtain a performance gain of 1.1% in JAC, 1.1% in AJI and 1.9% in PQ.

**Model Complexity** is typically measured by the amount of network parameters and FLOPs [35]. With the help of the proposed HVEC module, the parameters of our model are much less than that of U-Net (3.2 M vs. 31 M) and 3D U-Net (3.2 M vs. 19 M). Note that we follow the settings in [30], [6], and use four down-sampling stages in the U-Net and three down-sampling stages for 3D U-Net. In terms of computational complexity, our model takes about 97.7 GFLOPs, while 2D U-Net and 3D U-Net need 261.6 GFLOPs and 1244.3 GFLOPs, respectively. Although the size (3.2 M) of our model is higher than that (1.1M) of Xiao *et al.* [34], their 3D model takes 134.7 GFLOPs, which is higher than our model. Despite the significantly reduced parameters and computational complexity, our model shows state-of-the-art performance.

Besides, we have also tested the performance of our model with reduced feature channels and thus reduced parameters. Specifically, 1) when we reduce the number of channels after the second down-sampling operation from 256 to 192 and that

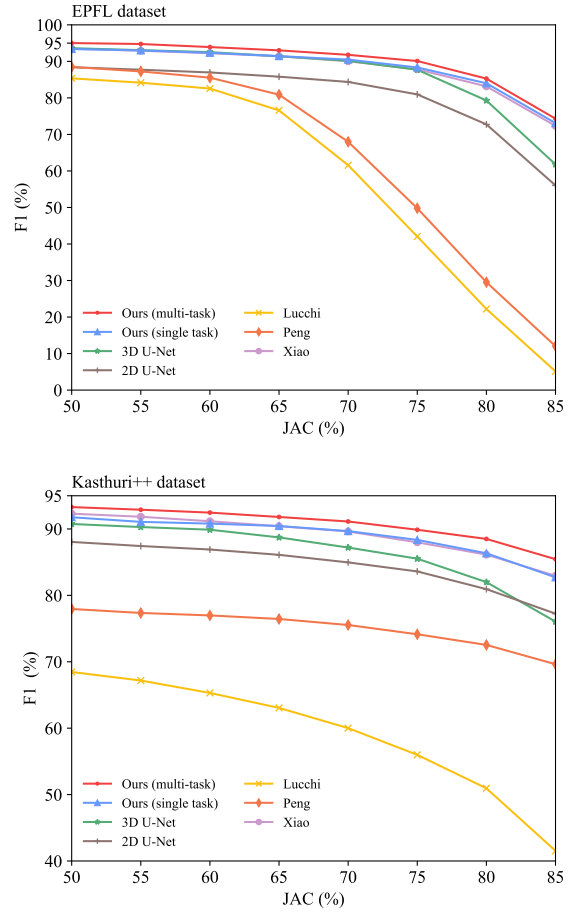


Figure 6: Detection performance in F1 with different overlapping thresholds for matched instances. The measure F1 is based on measuring the segment overlapping of matched instances.

after the third down-sampling operation from 512 to 256, we obtain a model with 1.27 M parameters with no loss of precision; 2) when we further reduce the number of channels after the third down-sampling operation to 192, we obtain a model with 1.04 M parameters with a performance loss of 0.05% in JAC on EPFL dataset; 3) when we further reduce the number of channels after the second down-sampling operation and that after the third down-sampling operation to 128, we obtain a model involving 0.69 M parameters and 70.1 GFLOPs but with a similar performance of 89.9% in JAC, that is a marginal performance loss of 0.2% in comparison with our full model (90.1% in JAC) on EPFL dataset. Moreover, we did not observe a loss of performance for instance-level segmentation in AJI (89.4%) and PQ(84.6%). These experimental results indicate that both our HVEC module and multi-task learning strategies are effective to improve segmentation performance.

#### 4.5. Detection performance

In addition to evaluate class-level and instance-level perfectness of the segmentation results, we also evaluate the detection performance under two class of measures. While the first class includes DQ, SEN and SPE that are based on the assessment



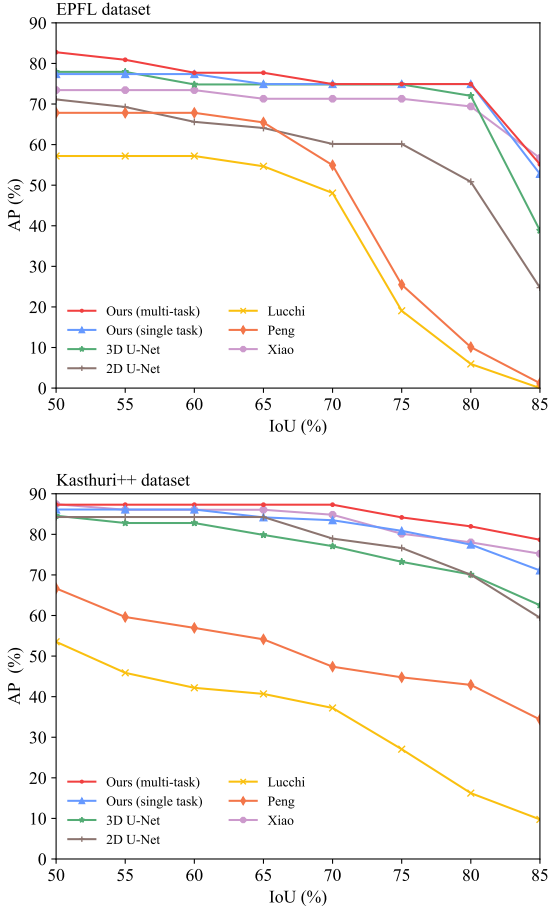


Figure 7: Detection performance in AP with different overlapping thresholds for matched instances. The AP is based on measuring the bounding-box overlapping (IoU) of matched instances.

of area overlapping of matched segments, the second class, i.e., AP, is based on the assessment of bounding-box overlapping of matched segments.

Table 3 and Table 4 have summarized the detection performance of different methods on EPFL dataset and Kasthuri++ dataset. The DQ/F1-50 and AP of our detection on both datasets outperforms all of the compared methods, which suggests the state-of-the-art performance of our method. Specifically, on the EPFL dataset, our model outperforms the method of Xiao *et al.* by 1.6% in DQ/F1-50 and 3.6% in AP-75; on the anisotropy Kasthuri++ dataset, our model outperforms the method of Xiao *et al.* by 1.0% in DQ/F1-50, and 4.1% in AP-75.

For completeness, we also conducted several experiments by considering different overlapping thresholds ranging from 50% to 85% for both F1 and AP on both datasets. The results are illustrated in Fig. 6 and Fig. 7. As shown in Fig. 6, our method yields better detection performance than the compared methods under varied thresholds. From Fig. 7, it can be seen that our method shows better results than other methods under most thresholds, especially on the more challenging Kasthuri++ dataset.

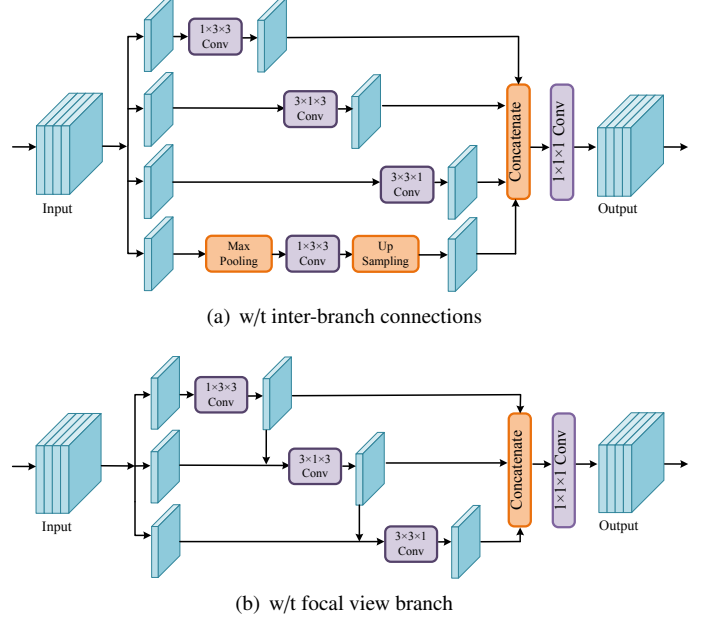


Figure 8: Illustration of ablated versions of the proposed HVEC block.

Table 5: Ablation study of architecture of the proposed HVEC block. The performance is evaluated on EPFL dataset.

| Experiments            |                          | A    | B    | C    | D           |
|------------------------|--------------------------|------|------|------|-------------|
| HVEC                   | Inter-branch connections | ✗    | ✗    | ✓    | ✓           |
|                        | Focal view branch        | ✗    | ✓    | ✗    | ✓           |
| HIVE-Net (single task) | JAC (%)                  | 88.1 | 88.8 | 88.5 | <b>89.2</b> |
|                        | DSC (%)                  | 93.7 | 94.1 | 93.9 | <b>94.3</b> |
| HIVE-Net (multi-task)  | JAC (%)                  | 89.2 | 89.8 | 89.5 | <b>90.1</b> |
|                        | DSC (%)                  | 94.3 | 94.6 | 94.4 | <b>94.8</b> |

#### 4.6. Ablation study of the proposed HVEC block

The proposed HVEC has a multi-branch architecture with hierarchical connections between neighboring branches and an additional branch is to extract multi-scale context on one focal view, as shown in Fig. 3. We conduct an ablation study to validate the effectiveness of two key components, i.e., *inter-branch connections*, and *focal view branch*, i.e., on the fourth branch in HVEC. Specifically, the experiments are conducted under four different settings: A) the HVEC using neither the *inter-branch connections* nor the *focal view branch*; B) the HVEC without *inter-branch connections* in Fig. 8 (a); C) the HVEC without *focal view branch* in Fig. 8 (b); D) the full HVEC in Fig. 3. The results are presented in Table 5.

As mentioned in Sect. 3.2, we use inter-branch connections in the HVEC, that is the feature maps produced by previous branch are added to the next branch as joint input, to enhance context feature extraction on each individual view and capture multi-scale fields-of-view. In fact, as discovered in many studies, multi-scale contexts [9, 33, 30] are crucial for accurate seg-

mentation. The effectiveness of the hierarchical inter-branch connections for mitochondria segmentation is confirmed by the performance gain, i.e., 0.4% performance gain in terms of JAC for our single-task model and 0.3% performance gain for our full multi-task model (as shown in Table 5).

With the additional convolutional branch on a specific view, we obtain an anisotropic model with a focal view as shown in Fig. 8 (b) and Fig. 3. The effectiveness of the focal view for mitochondria segmentation is confirmed by the performance gain, i.e., 0.7% performance improvement in JAC for our single-task model and 0.6% performance gain for our full multi-task model (as shown in Table 5). By the integration of the two key components, we obtain a performance gain of 1.1% in JAC for our single-task model and 0.9% performance gain for our full multi-task model. All these results show that the hierarchical inter-branch connections and focal view branch are critical to the performance of the proposed model.

#### 4.7. Sensitivity analysis of the trade-off hyper-parameter $\lambda$

The hyper-parameter  $\lambda$  in Eq. 3 is used to balance the main segmentation task and the auxiliary centerline detection task. Therefore, we conduct experiments to observe the impact of changing the trade-off value of  $\lambda$ . As depicted in Fig. 9, we present the curve of JAC about  $\lambda$  under different settings. Note that, when  $\lambda = 1$ , the full model degenerates to the single task version of our HIVE-Net. The choice of  $\lambda$  ranges from 1 to 0, and the proposed model achieves the best with a good balance of the two tasks with  $\lambda = 0.7$ . When  $\lambda = 0.1$ , the centerline detection task dominates the total loss and the performance has a sharp decrease. This indicates that giving too much emphasis on the auxiliary task will reduce the segmentation accuracy of our HIVE-Net.

#### 4.8. Effect of the number of training iterations

Since the number of training iterations usually has impact on the performance and over-training may lead to over-fitting, we conducted multiple runs of training with different number of iterations to check the stability of our results. From Fig. 10, it is clear that with more iterations, initially there is large performance gains. However, the performance gain becomes marginal after 300 epoch. To avoid over-fitting, we use early stopping and terminate the training with a maximum of 250 epochs.

#### 4.9. Impact of the amount of training data

We further investigate the segmentation performance of HIVE-Net method under limited annotated data circumstances. Specifically, we gradually reduce the amount of training data, and test on the same testing dataset, the result of which is depicted in Fig. 11. Predictably, as the decrease of training data, all methods demonstrate degenerated performance. Particularly, the 3D U-Net shows significant performance drop, and the gap between 3D U-Net and 2D U-Net narrows down quickly. However, our HIVE-Net and its single task variant are more robust to the reduction of training data, and is invariably higher

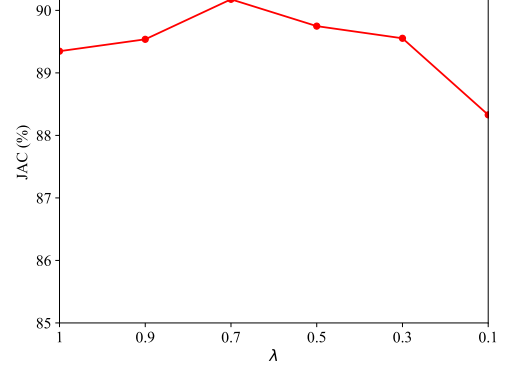


Figure 9: Impact of the parameter  $\lambda$  on the performance of our HIVE-Net.

than both 2D U-Net and 3D U-Net. Note that, when the training data reduce to only 30%, all of the baseline methods have a sharp drop below 80% in accuracy. In contrast, our method still can achieve sound performance, which confirms that the proposed HIVE-Net is an effective solution for mitochondria segmentation even in cases with scarce annotated training data.

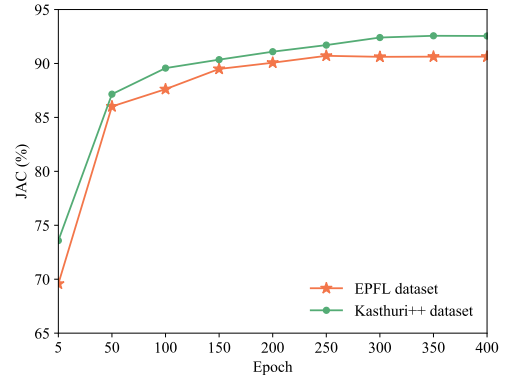


Figure 10: Effect of the number of training iterations on the performance of our model.

To further validate the robustness and generalization ability of our proposed model, we conduct the same experiments on Kasthuri++ dataset. With progressively decreased size of annotated training samples on Kasthuri++ dataset, as shown in Fig. 11, all methods show degenerated performance. On the Kasthuri++ dataset with anisotropic resolution, the 2D U-Net, segmenting the volume data slice by slice, shows more robust result, whereas the performance of 3D U-Net drops dramatically as the size of training data decrease. In contrast, even when the training data have decreased to 30%, our HIVE-Net still yields an accuracy over 89% in JAC. Moreover, our method is an end-to-end pseudo 3D model, and the input and output are both 3D image as that of the 3D U-Net.

## 5. CONCLUSION

In this paper, we have proposed an end-to-end-trainable shape-aware network for 3D segmentation of mitochondria

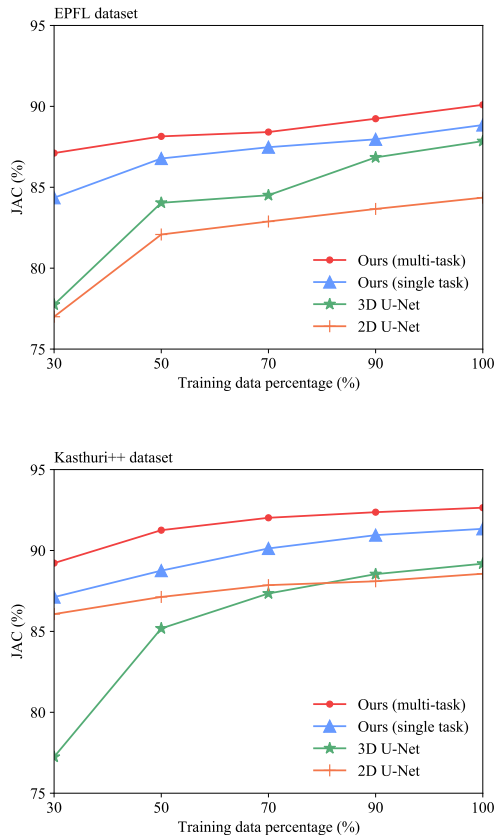


Figure 11: The comparative mitochondria segmentation performance on various fractions of training samples on EPFL dataset (top) and Kasthuri++ dataset (bottom).

from EM images. Besides of the main segmentation stream, our network explicitly accounts for intrinsic shape information by using a dedicated centerline detection stream. Further, the shared feature encoder between the two closely related tasks not only induces feature representations with better discriminability, but also improves the robustness and generalization ability of our model. We achieve a lightweight 3D segmentation model with fewer learnable parameters and low computation complexity by replacing 3D convolution with a novel HVEC module. Moreover, the proposed HEVC can be integrated with any 3D convolution network. Experiments show that our architecture can achieve state-of-the-art results on two challenging benchmarks, and shows significantly improved generalization ability even training with quite limited amount of training data.

A limitation of our HIVE-Net is that it only utilizes the centerline as shape knowledge, which may have little impact on boundary fitness of the segmentation result. In the future, the research could focus on 1) extending it to 2D networks while maintaining the ability; 2) extend it to weakly supervised scenario, where only dot annotations are available; 3) incorporating full shape knowledge in 2D variants.

## References

## References

- [1] Casser, V., Kang, K., Pfister, H., Haehn, D., 2018. Fast mitochondria segmentation for connectomics. *arXiv preprint arXiv:1812.06024*.
- [2] Cetina, K., Buenaposada, J.M., Baumela, L., 2018. Multi-class segmentation of neuronal structures in electron microscopy images. *BMC Bioinformatics* 19, 298.
- [3] Cheng, H.C., Varshney, A., 2017. Volume segmentation using convolutional neural networks with limited training data, in: *IEEE International Conference on Image Processing, IEEE*, pp. 590–594.
- [4] Cho, D.H., Nakamura, T., Lipton, S.A., 2010. Mitochondrial dynamics in cell death and neurodegeneration. *Cellular and Molecular Life Sciences* 67, 3435–3447.
- [5] Chollet, F., 2017. Xception: Deep learning with depthwise separable convolutions, in: *IEEE Conference on Computer Vision and Pattern Recognition*, pp. 1251–1258.
- [6] Çiçek, Ö., Abdulkadir, A., Lienkamp, S.S., Brox, T., Ronneberger, O., 2016. 3d u-net: learning dense volumetric segmentation from sparse annotation, in: *International Conference on Medical Image Computing and Computer-Assisted Intervention, Springer*, pp. 424–432.
- [7] Fakhry, A., Zeng, T., Ji, S., 2016. Residual deconvolutional networks for brain electron microscopy image segmentation. *IEEE Transactions on Medical Imaging* 36, 447–456.
- [8] Funke, J., Tschopp, F., Grisaitis, W., Sheridan, A., Singh, C., Saalfeld, S., et al., 2018. Large scale image segmentation with structured loss based deep learning for connectome reconstruction. *IEEE Transactions on Pattern Analysis and Machine Intelligence* 41, 1669–1680.
- [9] Gao, S., Cheng, M., Zhao, K., Zhang, X., Yang, M., Torr, P., 2020. Res2net: A new multi-scale backbone architecture. *IEEE Transactions on Pattern Analysis and Machine Intelligence*.
- [10] Gonda, F., Wei, D., Parag, T., Pfister, H., 2018. Parallel separable 3d convolution for video and volumetric data understanding. *arXiv preprint arXiv:1809.04096*.
- [11] Graham, S., Vu, Q.D., Raza, S.E.A., Azam, A., Tsang, Y.W., Kwak, J.T., Rajpoot, N., 2019. Hover-net: Simultaneous segmentation and classification of nuclei in multi-tissue histology images. *Medical Image Analysis* 58, 101563.
- [12] He, K., Zhang, X., Ren, S., Sun, J., 2016. Deep residual learning for image recognition, in: *IEEE Conference on Computer Vision and Pattern Recognition*, pp. 770–778.
- [13] Huo, Y., Xu, Z., Bao, S., Bermudez, C., Moon, H., Parvathaneni, P., et al., 2018. Splenomegaly segmentation on multi-modal mri using deep convolutional networks. *IEEE Transactions on Medical Imaging* 38, 1185–1196.
- [14] Kainz, P., Urschler, M., Schuster, S., Wohlfahrt, P., Lepetit, V., 2015. You should use regression to detect cells, in: *International Conference on Medical Image Computing and Computer-Assisted Intervention, Springer*, pp. 276–283.
- [15] Kasthuri, N., Hayworth, K.J., Berger, D.R., Schalek, R.L., Conchello, J.A., Knowles-Barley, S., et al., 2015. Saturated reconstruction of a volume of neocortex. *Cell* 162, 648–661.
- [16] Kingma, D.P., Ba, J., 2014. Adam: A method for stochastic optimization. *arXiv preprint arXiv:1412.6980*.
- [17] Kirillov, A., He, K., Girshick, R., Rother, C., Dollár, P., 2019. Panoptic segmentation, in: *Proceedings of the IEEE conference on computer vision and pattern recognition*, pp. 9404–9413.
- [18] Kumar, N., Verma, R., Sharma, S., Bhargava, S., Vahadane, A., Sethi, A., 2017. A dataset and a technique for generalized nuclear segmentation for computational pathology. *IEEE transactions on medical imaging* 36, 1550–1560.
- [19] Kumar, R., Vázquez-Reina, A., Pfister, H., 2010. Radon-like features and their application to connectomics, in: *2010 IEEE Computer Society Conference on Computer Vision and Pattern Recognition-Workshops, IEEE*, pp. 186–193.
- [20] Lin, T.Y., Maire, M., Belongie, S., Hays, J., Perona, P., Ramanan, D., Dollár, P., Zitnick, C.L., 2014. Microsoft coco: Common objects in context, in: *European conference on computer vision, Springer*, pp. 740–755.
- [21] Lucchi, A., Li, Y., Fua, P., 2013. Learning for structured prediction using approximate subgradient descent with working sets, in: *IEEE Conference on Computer Vision and Pattern Recognition*, pp. 1987–1994.

- [22] Lucchi, A., Smith, K., Achanta, R., Knott, G., Fua, P., 2011. Supervoxel-based segmentation of mitochondria in em image stacks with learned shape features. *IEEE Transactions on Medical Imaging* 31, 474–486.
- [23] Milletari, F., Navab, N., Ahmadi, S.A., 2016. V-net: Fully convolutional neural networks for volumetric medical image segmentation, in: 2016 Fourth International Conference on 3D Vision (3DV), IEEE. pp. 565–571.
- [24] Nunnari, J., Suomalainen, A., 2012. Mitochondria: in sickness and in health. *Cell* 148, 1145–1159.
- [25] Paszke, A., Gross, S., Massa, F., Lerer, A., Bradbury, J., Chanan, G., et al., 2019. Pytorch: An imperative style, high-performance deep learning library, in: *Advances in Neural Information Processing Systems*, pp. 8024–8035.
- [26] Peng, J., Yuan, Z., 2020. Mitochondria segmentation from em images via hierarchical structured contextual forest. *IEEE Journal of Biomedical and Health Informatics* 24, 2251–2259.
- [27] Perez, A.J., Seyedhosseini, M., Deerinck, T.J., Bushong, E.A., Panda, S., Tasdizen, T., et al., 2014. A workflow for the automatic segmentation of organelles in electron microscopy image stacks. *Frontiers in Neuroanatomy* 8, 126.
- [28] Prasoon, A., Petersen, K., Igel, C., Lauze, F., Dam, E., Nielsen, M., 2013. Deep feature learning for knee cartilage segmentation using a triplanar convolutional neural network, in: *International Conference on Medical Image Computing and Computer-Assisted Intervention*, Springer. pp. 246–253.
- [29] Qiu, Z., Yao, T., Mei, T., 2017. Learning spatio-temporal representation with pseudo-3d residual networks, in: *IEEE International Conference on Computer Vision*, pp. 5533–5541.
- [30] Ronneberger, O., Fischer, P., Brox, T., 2015. U-net: Convolutional networks for biomedical image segmentation, in: *International Conference on Medical Image Computing and Computer-Assisted Intervention*, Springer. pp. 234–241.
- [31] Seyedhosseini, M., Ellisman, M.H., Tasdizen, T., 2013. Segmentation of mitochondria in electron microscopy images using algebraic curves, in: *IEEE 10th International Symposium on Biomedical Imaging*, IEEE. pp. 860–863.
- [32] Smith, K., Carleton, A., Lepetit, V., 2009. Fast ray features for learning irregular shapes, in: *IEEE International Conference on Computer Vision*, pp. 397–404.
- [33] Szegedy, C., Vanhoucke, V., Ioffe, S., Shlens, J., Wojna, Z., 2016. Rethinking the inception architecture for computer vision, in: *IEEE Conference on Computer Vision and Pattern Recognition*, pp. 2818–2826.
- [34] Xiao, C., Chen, X., Li, W., Li, L., Wang, L., Xie, Q., et al., 2018. Automatic mitochondria segmentation for em data using a 3d supervised convolutional network. *Frontiers in Neuroanatomy* 12, 92.
- [35] Xie, S., Girshick, R., Dollár, P., Tu, Z., He, K., 2017. Aggregated residual transformations for deep neural networks, in: *IEEE conference on Computer Vision and Pattern Recognition*, pp. 1492–1500.
- [36] Xie, Y., Zhang, J., Lu, H., Shen, C., Xia, Y., 2020. Sesv: Accurate medical image segmentation by predicting and correcting errors. *IEEE Transactions on Medical Imaging*.
- [37] Yuan, Z., Yi, J., Luo, Z., Jia, Z., Peng, J., 2020. Em-net: Centerline-aware mitochondria segmentation in em images via hierarchical view-ensemble convolutional network, in: *2020 IEEE 17th International Symposium on Biomedical Imaging (ISBI)*, IEEE. pp. 1219–1222.
- [38] Zeng, T., Wu, B., Ji, S., 2017. Deepem3d: approaching human-level performance on 3d anisotropic em image segmentation. *Bioinformatics* 33, 2555–2562.
- [39] Zhang, J., Xie, Y., Zhang, P., Chen, H., Xia, Y., Shen, C., 2019. Light-weight hybrid convolutional network for liver tumor segmentation., in: *IJCAI*, pp. 4271–4277.
- [40] Zhao, X., Wu, Y., Song, G., Li, Z., Zhang, Y., Fan, Y., 2018. A deep learning model integrating fcnn and crfs for brain tumor segmentation. *Medical Image Analysis* 43, 98–111.